Micro-cold Spray Deposition of YSZ Films from Ultrafine Powders Using a Pressure Relief Channel Nozzle

Stephen G. Bierschenk[1,2] (iD) · Desiderio Kovar[1,2]

Abstract The use of ultrafine powders in the micro-cold spray (MCS) process, also referred to as the aerosol deposition method, typically results in porous and/or poorly adhering films because the particles do not impact at a high enough velocity for sufficient plastic deformation and interparticle bonding to occur. Under typical operating conditions, particles < 100 nm accelerate to high velocities but then are slowed by the stagnant gas in the bow shock that forms just upstream of the substrate. Using larger particles reduces particle slowing, but large particles can cause erosion of the film at high impact velocity, decreasing deposition efficiency. In this study, a pressure relief channel nozzle using helium as a carrier gas is proposed such that high-velocity deposition of yttria-stabilized zirconia particles as small as 10 nm in diameter is possible. This is well below the size range of powders previously used for MCS. The proposed nozzle design increases impact velocities for 10, 20, and 50 nm particles by ∼ 880, 560, and 160 m/s, respectively, when compared to a conventional nozzle. Experimental deposition of ultrafine 8YSZ powder shows that the pressure relief channel nozzle results in lower porosity and more uniform deposits, with a ∼ 186% increase in deposition efficiency.

✉ Desiderio Kovar
   dekovar@austin.utexas.edu

   Stephen G. Bierschenk
   bierschenk@utexas.edu

1 Department of Mechanical Engineering, University of Texas at Austin, Austin, TX 78712, USA

2 Center for Additive Manufacturing in Design Innovation, University of Texas at Austin, Austin, TX 78712, USA

Introduction

Spray coating of metal and ceramic films produced from a feedstock of aerosolized dry particles via micro-cold spray (MCS), also referred to as the aerosol deposition method and vacuum kinetic spraying, has been widely studied in recent years (Ref 1-5). The particles are entrained in a low pressure 26.7-101 kPa (200-760 Torr) carrier gas and accelerated through a nozzle into a vacuum chamber 0.13-1.3 kPa (1.0-10 Torr). Upon impact with a room temperature substrate, particles deform and adhere to form a solid film with thicknesses of 1-100 μm.

Particles must impact with sufficient velocity to plastically deform and produce high density, adherent films. Finer particles can be easily accelerated to high velocities because of their large drag-to-mass ratio, but they are then slowed by the stagnant gas in the bow shock that forms upstream of the substrate for typical operating conditions used in MCS. The low impact velocities for fine powders < 100 nm in diameter with conventional nozzle geometries often lead to poorly adherent and/or low-density films (Ref 6-8). Larger ceramic particles have sufficient momentum that they are not strongly affected by the bow shock, but their impact can cause erosion of the previously deposited films and underlying substrate. Thus, in practice, particles that have been used for MCS to date have diameters between 100 nm and 2 μm. Additionally, recent molecular dynamics studies of single nanoparticle impacts have indicated that, at sufficiently high impact velocities, particles < 50 nm in diameter can deform and

adhere without fracture (Ref 9-12). Larger particles that are currently used typically fracture upon impact with large portions of the fractured particle removed in the gas stream (Ref 13). The deposition of finer particles at high velocity should improve deposition efficiency by both reducing erosion and increasing the fraction of each particle that adheres to the substrate.

We recently proposed a methodology for designing nozzles that contain a pressure relief channel that allows the gas pressure within the stagnation region to be substantially reduced (Ref 14). The introduction of the pressure relief channel particularly benefits the impact velocities for finer particles because they slow less in the stagnation region than they would with a conventional nozzle. It was previously shown that this new nozzle design, when used with nitrogen carrier gas, allowed particles as small as 50 nm to be deposited at impact velocities > 450 m/s, improving deposition efficiency for a yttria-stabilized zirconia (YSZ) powder with a broad particle size distribution. For particles < 50 nm in diameter, however, the relatively high density of the nitrogen carrier gas in the stagnation region slowed particles to velocities too slow for deposition.

In this paper, we investigate the use of a pressure relief channel nozzle in combination with helium carrier gas to deposit yttria-stabilized zirconia (YSZ) particles that have a nominal mean size of < 50 nm, but with a relatively wide dispersion in particle/agglomerate sizes. Numerical studies are performed to predict the particle impact velocities with helium gas for particles as small as 10 nm. Experiments are conducted to compare deposits produced using the pressure relief channel nozzle to deposits produced with a conventional converging–diverging nozzle.

Methodology

Nozzle Geometries

A geometry for the pressure relief channel nozzle was determined in a previous study that showed it produced low gas pressures in the bow shock region and significantly increased particle impact velocities and deposition efficiency for fine 8YSZ particles in a nitrogen gas (Ref 14). The outer geometry and cross-section of the nozzle used to manufacture a prototype are shown in Fig. 1(a) and (b), respectively. The pressure relief channels in the side of the diverging region allow gas to be removed from nozzle, lowering the pressure in the downstream bow shock. Three, thin support features, concentric about the nozzle axis and visible in Fig. 1(a), are presented within the pressure relief channels to connect the upper and lower portions of the nozzle. The cross-section in Fig. 1(b) shows that the
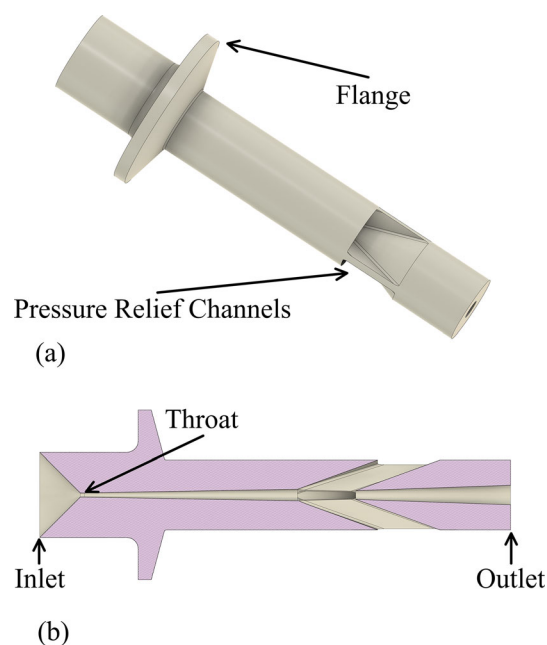

Fig. 1 (a) Outer and (b) cross-sectional views of a three-dimensional model of the pressure relief channel nozzle

portion of the diverging region between pressure relief channels and the nozzle outlet is slightly inset to encourage gas diversion away from the nozzle axis.

Previous work determined that a two-dimensional approximation of the nozzle geometry that is symmetric about the axis and ignores the support features within the pressure relief channels provides a reasonable approximation for numerically calculated gas and particle velocities when compared to a three-dimensional geometry with support structures included (Ref 14). Due to the high computational cost of performing three-dimensional computational fluid dynamics (CFD) studies that can accurately model the relevant gas flow, a two-dimensional approximation is used in this work.

The pressure relief channel nozzle geometry used for the CFD simulations is shown in Fig. 2(a). Additionally, a converging–diverging nozzle with a similar geometry to those currently used in cold spray and micro-cold spray (Ref 15) is defined in Fig. 2(b) to compare with the pressure relief channel nozzle. For both nozzle geometries, a 40 mm long, 10 mm radius inlet region converges to a 1-mm-diameter nozzle throat. The respective geometries result in outlet diameters of approximately 8.0 mm for the conventional converging–diverging nozzle and 4.6 mm for the pressure relief channel nozzle. Downstream of the nozzle exit is a 40-mm-wide substrate, depicted as a vertical blue line, with a 110-mm-long outlet that is parallel to the nozzle axis and starts at the outer substrate edge. The length of the nozzle diverging region, L_1, is set to 100 mm. The dimensions listed for the pressure relief channel

(a) Pressure Relief Channel Geometry
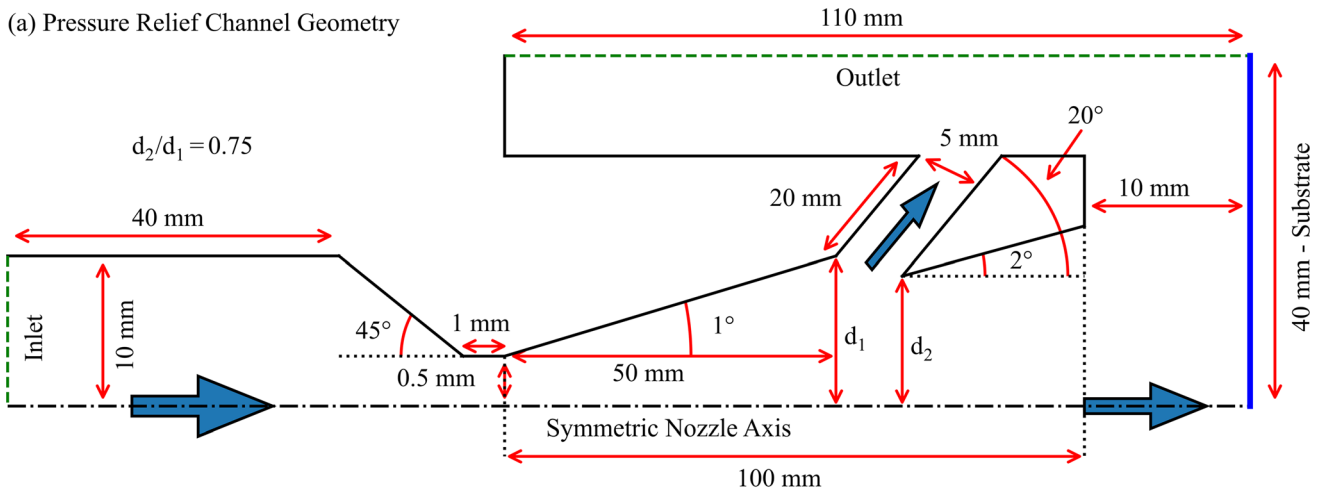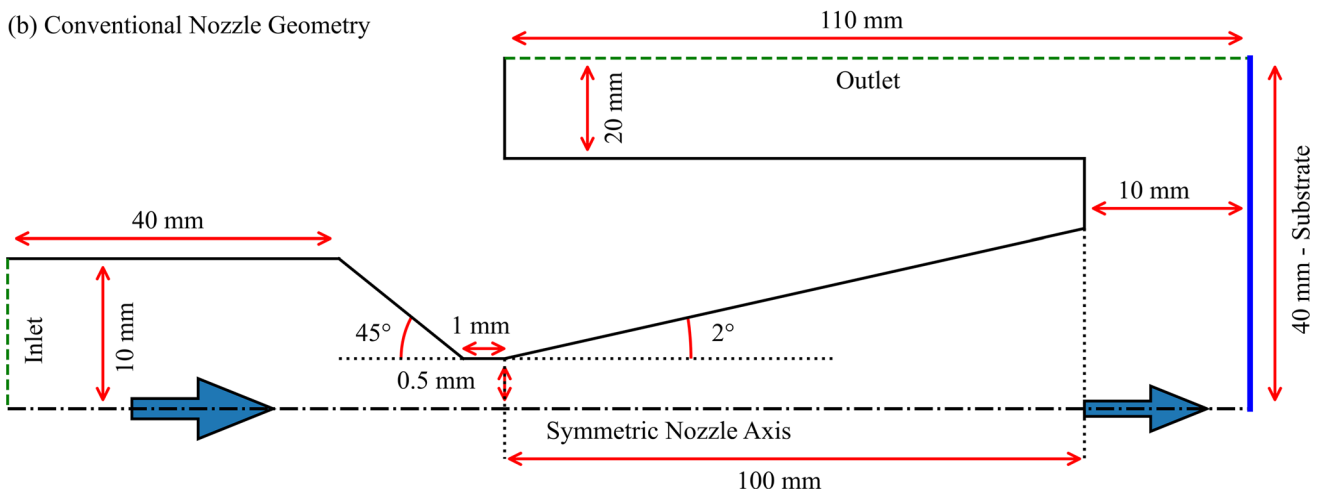

(b) Conventional Nozzle Geometry

Fig. 2 Two-dimensional geometry employed in the CFD simulations for the (a) pressure relief channel nozzle and the (b) conventional converging–diverging nozzle geometry. Solid black lines represent the boundaries of the nozzle or deposition system, and the solid blue line is the substrate. The green-dashed lines represent the inlet (left), outlet (top), and the dash-dotted line represents the symmetric nozzle axis (bottom) (Color figure online)

geometry in Fig. 2(a) are identical to those determined in previous work (Ref 14) and used for the manufactured nozzle as shown in Fig. 1.

Computational Fluid Dynamics Analysis for Gas Velocities

The gas flow profile for all nozzles was obtained using the CFD module of the COMSOL Multiphysics® software package (Ref 16). Parameters for the time-dependent solver, boundaries, and mesh for the CFD simulations were similar to those in previous work (Ref 14, 17). Gas flow through the nozzle was calculated using the two-dimensional, fully compressible Navier-Stokes equations. The temperature dependence of the gas viscosity was approximated using Sutherland's law, and heat transport was calculated using the Kays–Crawford model. Details on the implementation of these models can be found in the COMSOL CFD User Guide (Ref 18). The Spalart–Allmaras turbulence model (Ref 19), previously used to accurately model turbulence in supersonic gas flows through a nozzle (Ref 20), was used to model any turbulence that may arise in the simulation. A time-dependent solver was used to reach an approximately steady state flow. Flow became close to steady state at approximately 1 ms, but the simulations were carried out to 3 ms for each nozzle geometry. A fine, triagonal mesh with a maximum element edge length of 0.05 mm in the shock wave regions has been shown previously to be of sufficient density to accurately calculate the flow field (Ref 14, 17). The thin boundary layers in the gas flow along the walls of the nozzles were refined using the COMSOL boundary layer mesh function which adds a layer of dense quadrilateral mesh elements. This meshing scheme is described in detail

in the COMSOL CFD user guide (Ref 16). The effects of inlet pressure, outlet pressure, and nozzle-to-substrate distance on gas and particle velocity are well documented in other studies (Ref 21-25). For this reason, analysis in this study was limited to a single pressure with static inlet and outlet pressures of 40 kPa (300 torr) and 0.13 kPa (1 torr), respectively, and a nozzle-to-substrate distance of 10 mm. Simulations were two-dimensional and symmetric about the nozzle axis. Helium was used as the carrier gas.

Numerical Analysis of Particle Velocities

The gas velocity, density, temperature, and viscosity were determined from the solution of the CFD simulation at each node of the finite element mesh. Using the two-dimensional equation for particle motion and the particle drag relations developed by Li et al. (Ref 26), the trajectory and velocity of 20, 50, and 100 nm particles were calculated from the nozzle inlet to their impact on the substrate. Because the gas velocity upstream of the nozzle inlet is low enough that the choice of particle velocity is not critical to the calculation, each particle was given an arbitrary but realistic initial velocity of 95% of the gas velocity. At each step in the trajectory, gas properties were calculated via linear interpolation between the data points exported from the CFD solution. For these calculations, it was assumed that particles were spherical, solid particles with a density of 5.9 g/cm^3 (the density of 8YSZ). In addition, it was assumed that the gas and particle surface were at the same temperatures and that the particles did not perturb the gas flow field.

Experimental Procedures

Using the parameters determined in a previous study (Ref 14) and shown in Fig. 2(a), the pressure relief nozzle shown in Fig. 1 was fabricated out of Nylon 12 using selective laser sintering (SLS) at UT Austin's Center for Additive Manufacturing and Design Innovation (CAMDI). A traditional converging–diverging nozzle whose geometry is shown in Fig. 2(b) was also fabricated in the same manner for comparison. Images of the SLS-manufactured nozzles are shown in the supplementary material of the previous study (Ref 14).

The powder used for this study was 8YSZ with an average primary particle size of 40 nm, as reported by the manufacturer (Tosoh TZ-8Y, Tokyo, Japan). Five measurements of the average feed rate exiting the feeder were conducted by weighing the mass of fed powder every 5 s over a period of 5 min. The feed rate was determined to be 0.16 ± 0.01 g/min. The powder and helium carrier gas were directed into a deagglomerator which subjected the particles to high-shearing forces, which aerosolized them

and broke apart soft agglomerates. The gas/particle mixture was then accelerated through the nozzle into a vacuum chamber onto a substrate affixed to an x-y-z motion stage. Schematics of the MCS set-up have been published previously (Ref 4) along with detailed designs of the feeder and deagglomerator (Ref 27). For the current experiments, the nozzle exit-to-substrate distance was fixed at 10 mm and single crystal, polished silicon substrates were used as the substrate. The 8YSZ film was deposited by scanning the substrates back and forth beneath the nozzle in a straight line 20 times at a scan speed of 10 mm/s. The gas flow rate was set to 10 slpm, which resulted in gas pressures upstream of the nozzle inlet of ∼ 33 kPa for the traditional converging–diverging nozzle and ∼ 37 kPa for the pressure relief channel nozzle. The deposition chamber pressure for all tests was < 0.075 kPa.

Cross sections of the resulting films were prepared using a broad beam argon ion mill for 30 min under an accelerating voltage of 6 kV and an ion beam current of 0.3 mA (IM4000C broad beam ion milling system, Hitachi, Ltd., Tokyo, Japan). Samples were sonicated in deionized water before and after cross sectioning to remove any loose powder or non-adherent portions of the film. Cross-sectional images of the films were obtained using a scanning electron microscope (SEM). Additionally, profiles and surface roughness of the films deposited with each nozzle were obtained using digital microscopy (VHX-7000, Keyence Corporation-film profiles, Zeta-20, KLA Corporation-surface roughness).

Results

Simulation Results

The calculated particle impact velocities are plotted versus the impacting particle size on a linear-log scale in Fig. 3. This plot confirms that the calculated particle impact velocities for particle sizes < 100 nm for the pressure relief nozzle geometry are significantly greater compared to the impact velocities for traditional converging–diverging nozzle. For example, impact velocities of > 800 m/s are predicted for a 10 nm particle when using the improved nozzle whereas this size particle is not predicted to impact at all when using a traditional nozzle. The differences between the predicted impact velocities for the improved versus traditional nozzle decrease with particle size so that as the particle size approaches 100 nm, the differences between the nozzles are negligible.

Plots of velocity magnitude within the conventional nozzle and pressure relief channel nozzle are shown in Fig. 4(a) and (b), respectively. Negligible differences in gas velocities are observed within the nozzles; however, a large

fraction of the gas is diverted away from the main gas stream in the pressure relief channel nozzle. This diversion of gas leads to a significant decrease in gas pressure within the bow shock region. Pressure contours in a magnified, 5 mm × 5 mm view directly upstream of the substrate are
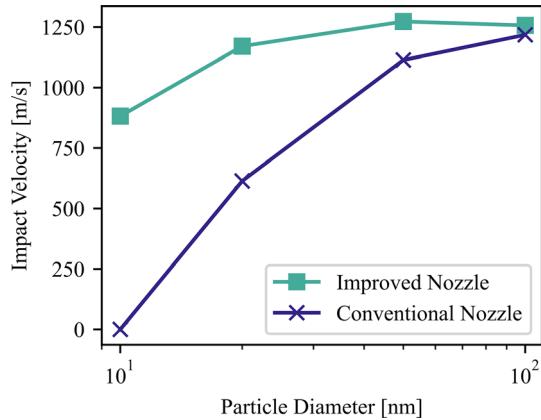

Fig. 3 Comparison of particle impact velocities versus particle size (log scale) predicted for the improved nozzle and the conventional nozzle. Calculations were performed for 8YSZ particles using helium as the carrier gas at an upstream pressure of 40 kPa and a chamber pressure of 0.13 kPa

shown in Fig. 4(c) and (d). For the conventional nozzle (Fig. 4c), a bow forms shock 2.9 mm above the substrate surface with a maximum pressure of 7.5 kPa. In contrast, the bow shock occurs at approximately 1.2 mm from the substrate surface (Fig. 4d), and the gas reaches a maximum pressure of 4.9 kPa for the pressure relief nozzle. Due to the similarities in gas velocities within the nozzle, particles reach the bow shock at similar velocities. However, the thinner, lower pressure stagnant gas below the bow shock for the pressure relief channel nozzle allows particles < 100 nm to maintain the much higher velocities observed in Fig. 3.

The gas velocity, temperature, pressure, and Mach number along the central axis of each nozzle are examined in Fig. 5. Due to the slightly larger diverging angle for the conventional nozzle, gas velocity increases and gas pressure decreases at a higher rate between the nozzle throat and the midway point of the diverging region as shown in Fig. 5(a) and (c). At the location of the pressure relief channel, a small decrease in pressure is observed corresponding with a decrease in temperature and significant increases in gas velocity and Mach number for the improved nozzle. Directly upstream of the bow shock, a decrease in gas velocity and Mach number to slightly
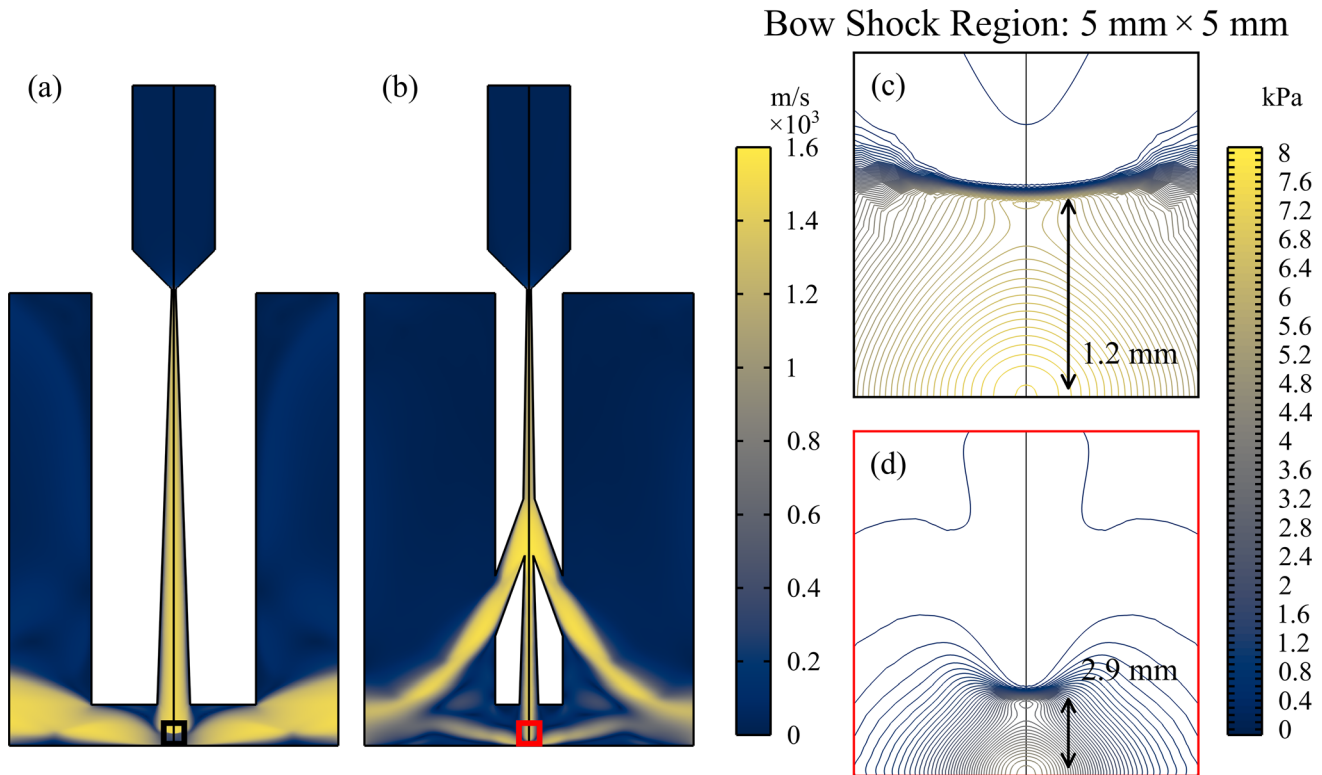

Fig. 4 The velocity magnitude of the helium gas within the (a) conventional and (b) pressure relief channel nozzle. Magnified views of the pressure contours in the bow shock for the (c) conventional and (d) pressure relief channel nozzle. The black and red boxes

in (a) and (b) show the regions that are magnified in (c) and (d), respectively. The vertical black line along the center of each plot represents the symmetric nozzle axis (Color figure online)
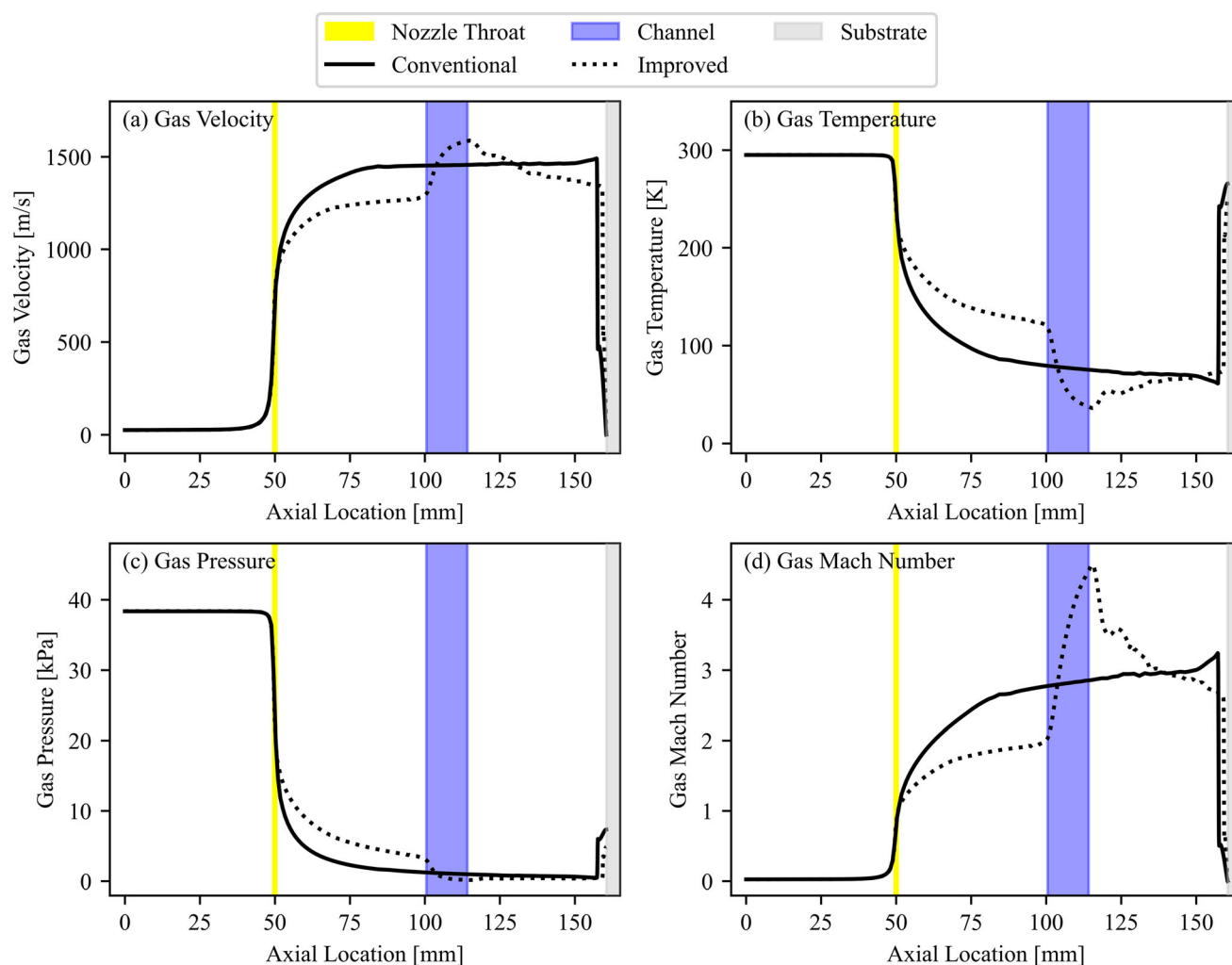
Fig. 5 The gas (a) velocity, (b) temperature, (c) pressure, and (d) Mach number along the central axis of the conventional and improved pressure relief channel nozzles. The location of the nozzle throat (yellow), pressure relief channel (blue), and substrate (gray) are indicated in each plot (Color figure online)

below that of the conventional nozzle is observed for the pressure relief channel nozzle. As fine particles are easily accelerated by the carrier gas, particle velocities upstream of the bow shock should be similar between the two nozzles. As the gas passes the bow shock and reaches the substrate, the gas stagnates. This results in a sharp drop in gas velocity and Mach number to near zero, and corresponding increases in pressure and temperature are observed. The lower pressure within the stagnation region for the pressure relief channel nozzle allows particles to maintain a higher impact velocity.

The removal of gas through the pressure relief channel can also have significant effects on particles that are not traveling along the central axis of the nozzle. To study these effects, calculations were performed for 20, 50, and 100 nm-diameter particles with initial radial locations from 0 to 9 mm from the nozzle axis, and their trajectories are shown in Fig. 6. This plot shows that 20 nm-diameter

particles are well focused in the upper portion of the diverging region, but defocus as they pass the pressure relief channels. Since they are focused in the center of the stream as they near the pressure relief channel region, all particles continue through the nozzle and impact on the substrate with the exception of the particle with an initial radial location of 9 mm which defocuses to such a degree that it impacts on an inner wall of the nozzle near the nozzle exit. The 50 nm particles are also well focused, and due to their larger mass, experience less defocusing when passing the pressure relief channel. For the largest 100 nm-diameter particles, significant overfocusing near the nozzle throat is observed. This overfocusing, combined with the defocusing effects of the pressure relief channels, causes particles with radial locations > 4 mm to impact on the nozzle walls or be diverted through the channels.

The degree to which particles focus within the nozzle can significantly affect their impact velocities. Figure 7
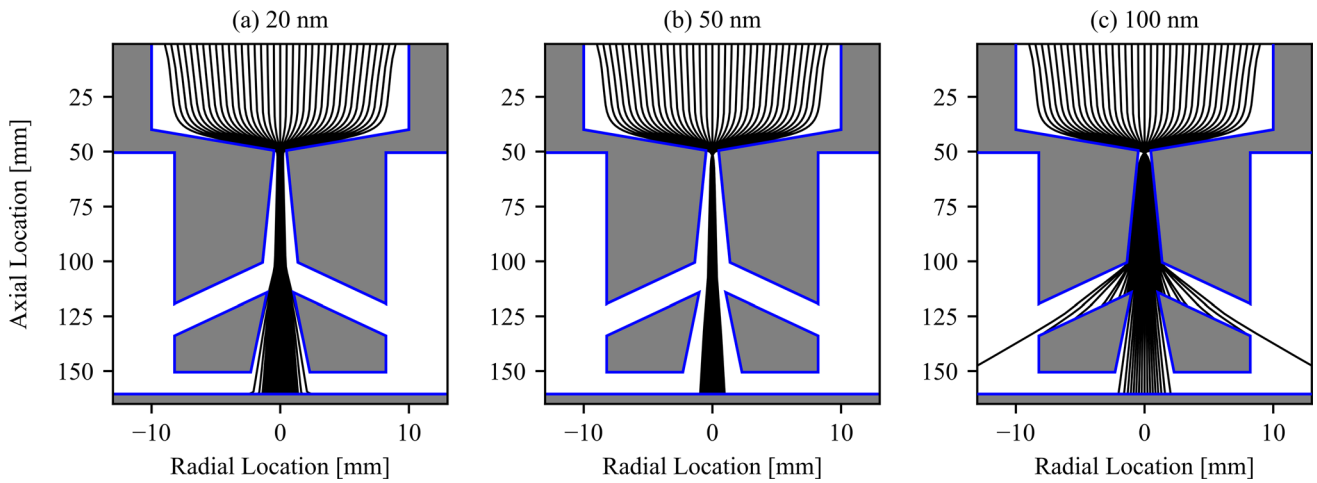
Fig. 6 Particle trajectories for (a) 20 nm, (b) 50 nm, and (c) 100 nm particles for the improved pressure relief channel nozzle design using helium as the carrier gas with an upstream pressure of 40 kPa and a chamber pressure of 0.13 kPa
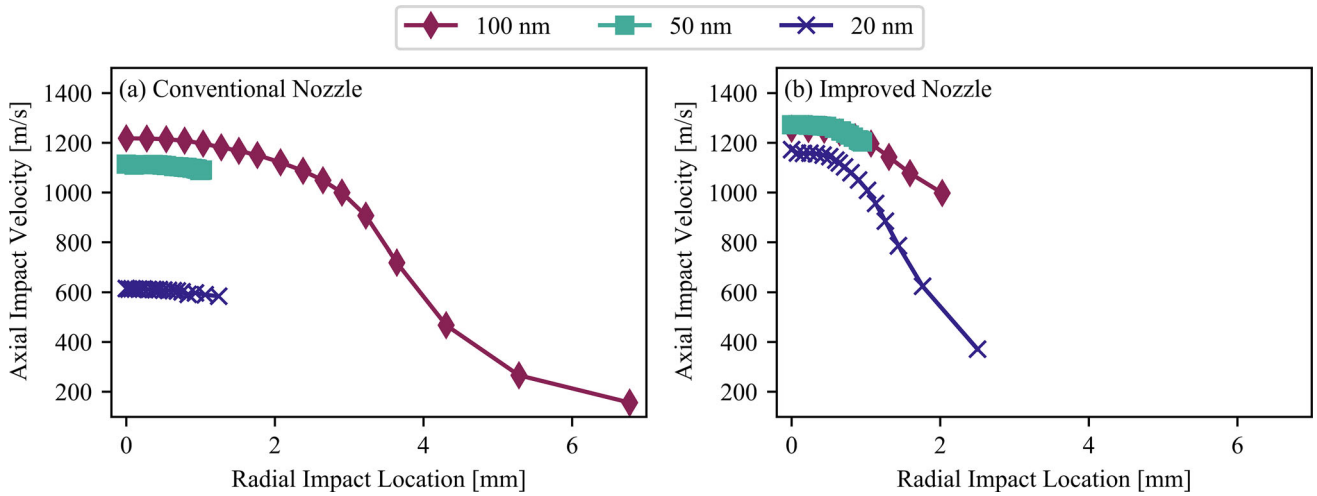

Fig. 7 Particle normal impact velocity versus radial impact location for the (a) conventional converging–diverging nozzle and (b) improved pressure relief channel nozzle for particle sizes of 20-100 nm using helium as the carrier gas with an upstream pressure of 40 kPa and a chamber pressure of 0.13 kPa

shows that the normal axial impact velocities at non-zero radial impact locations can vary by up to 1000 m/s when comparing the conventional and pressure relief channel nozzle. For the conventional converging–diverging nozzle, the axial impact velocities for 20 and 50 nm particles vary minimally as the radial impact location increases since both particle diameters focus to within 2 mm of the nozzle axis. The 100 nm particles overfocusing significantly, similar to what is shown in Fig. 6(c) with the pressure relief channel nozzle, but a much larger portion of particles impacts since no pressure relief channel is present to divert particles out of the flow. The overfocused 100 nm particles maintain high axial impact velocities until radial impact locations exceed 3 mm away from the nozzle axis. For the pressure relief channel nozzle, the diversion of gas flow away from the nozzle axis pulls the smaller 20 nm particles away from

the nozzle centerline as shown in Fig. 6(a). This leads to a drop-off in impact velocities for particles accelerated using the pressure relief channel nozzle that is not observed with a conventional nozzle for 20 nm particles impacting > 1 mm away from the nozzle axis. The overfocusing that occurs for 100 nm particles leads to a small drop-off in impact velocity for impact locations up to about 2 mm, similar to the drop-off in impact velocities for the conventional nozzle. However, the large drop-off in impact velocity at large radial distances observed in Fig. 7(a) with the conventional nozzle is not observed for the pressure relief channel nozzle because the particles located at large radial distances in the flow are diverted into the pressure relief channels. The channels effectively act like an aperture that removes particles at larger radial distances in the flow.

Experimental Results

Representative SEM images of the as-received powder and the powder after it had passed through the high-shear deagglomerator, but before it was accelerated through the nozzle are shown in Fig. 8(a) and (b). Figure 8(a) shows a mix of large and small agglomerates along with some unagglomerated primary particles in the as-received sample. Figure 8(b) shows the absence of large agglomerates, because they were broken apart by the high-shear deagglomerator. However, many small agglomerates are still present, along with many individual primary particles. The agglomerates have a lower density relative to the bulk 8YSZ (Ref 4) and thus would be expected to experience significantly more deceleration in the bow shock than similarly sized dense particles.
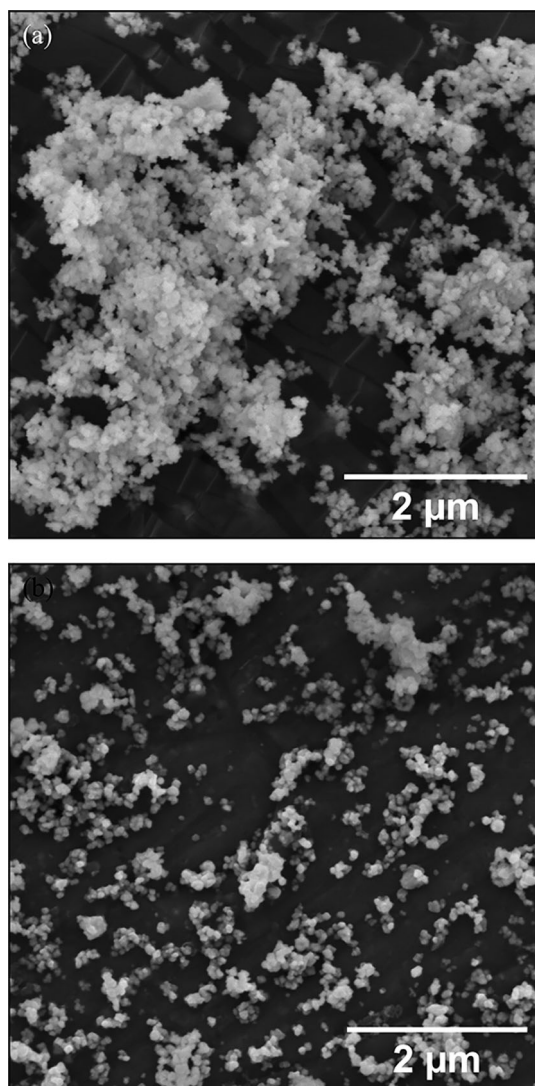
Following deposition of films using each nozzle, representative cross sections at the center of the deposited line were prepared to study the coating thickness and morphology. The cross sections are shown in Fig. 9. The coatings deposited using the pressure relief nozzle are significantly thicker, $\sim 13\ \mu m$, compared to the coatings deposited with the traditional converging–diverging nozzle, $\sim 5\ \mu m$. Variations in film thickness are observed in the film deposited using a conventional converging–diverging nozzle that are not presented in the film produced using the pressure relief channel nozzle. This is likely due to the build-up of loosely compacted powder in some areas of the film as is typical of films deposited using conventional nozzles and ultrafine ceramic powders (Ref 6-8). This loose powder does not adhere strongly to the substrate

Fig. 8 Morphology of the powder (a) as-received and (b) after passing through the high-shear deagglomerator
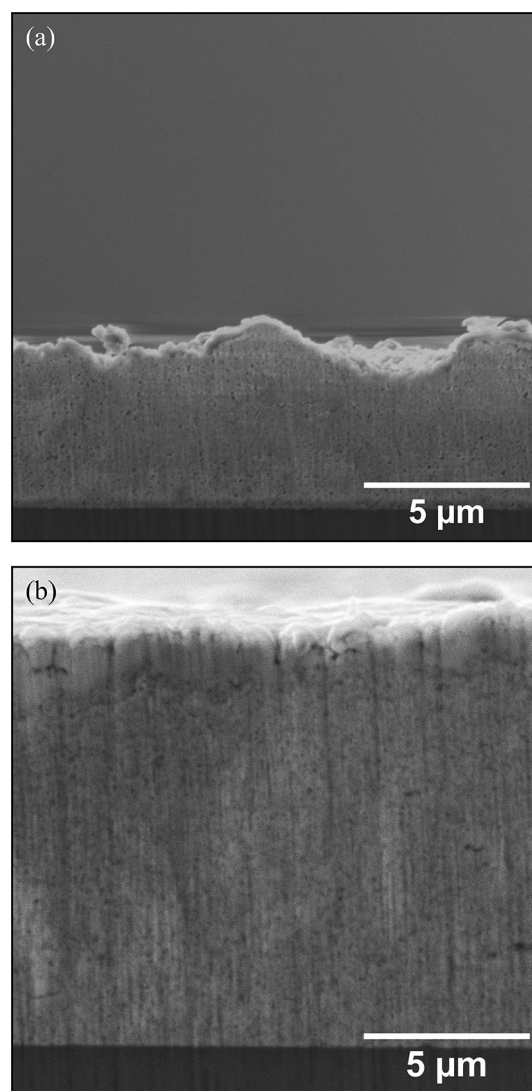

Fig. 9 SEM images of cross sections for films produced using (a) converging–diverging nozzle and (b) improved pressure relief channel nozzle

and is removed during sonication, leaving behind uneven film thicknesses and porosity.

To better understand the deposition efficiency, the films were examined using optical microscopy and profilometry. Figure 10(a) shows plan-view optical images of the deposited 8YSZ lines. The line patterns deposited with the improved nozzle are narrower than those produced with the conventional nozzle. Lines deposited with the traditional converging–diverging nozzle are wider and visibly less opaque. The difference in line width can be mostly attributed to the difference in outlet diameters of the two nozzles. For the improved nozzle, the initial diverging angle is 1°, while the conventional nozzle has a diverging angle of 2°. This leads to small differences in particle focusing behavior within the upper portion of the nozzle diverging regions observed in Fig. 6 but has a small effect on gas velocities near the nozzle exit and thus on particle velocities prior to crossing the bow shock. The lower portion of the diverging region of the improved nozzle is slightly inset, further reducing the outlet diameter. This results in outlet diameters of 4.6 and 8 mm for the improved nozzle and the conventional converging–diverging nozzle, respectively. These outlet diameters closely match the observed film widths, indicating that the particles and agglomerates shown in Fig. 8(a) are dispersed across the width of the nozzle during deposition. Since the films produced using the conventional nozzle have a larger width, they are also thinner. This difference in thickness observed in Fig. 9 is likely a contributing factor in the difference in opacity between the two films; however, slight differences in film density could be a contributing factor.

Eight separate profile measurements were obtained for each film. The average cross-sectional profile for each film is shown in Fig. 10(b). Average cross-sectional areas of 14,790 μm^2 and 27,510 μm^2 with standard deviations of 1750 μm^2 and 2600 μm^2 were measured for the films produced with the conventional nozzle and pressure relief channel nozzle, respectively, indicating an increase in deposition efficiency of 186% for the improved nozzle.

Ten surface roughness measurements were taken over randomly selected 212×159 μm (100× magnification) regions near the center of each film. Film surface roughness (Sa) was determined to be 0.45 ± 0.04 μm for the film deposited with the conventional nozzle and 0.31 ± 0.01 μm for the film deposited with the improved nozzle. These measurements confirm the results from the cross-sectional images as shown in Fig. 9 which indicates a smoother and more consistent film thickness for the film deposited with the improved nozzle.

Discussion

We have considered the effects only of drag forces on particle velocities in this study. The effects on particle velocity of other forces such as the Saffman lift force, pressure gradient force, Magnus force, and thermophoretic force have been examined in previous publications, and it is appropriate to discuss them in the context of the present study (Ref 28, 29). The pressure gradient and Magnus forces are expected to be several orders of magnitude smaller than the drag force and were therefore neglected in this study (Ref 28). The Saffman lift force has been shown

Fig. 10 (a) Optical images of the films deposited using the pressure relief channel nozzle (left) and the conventional converging–diverging nozzle (right) and (b) average cross-sectional profiles of deposited films. Average cross-sectional area (M) and standard deviation (SD) for films deposited with each nozzle are included in the figure legend

— Improved Nozzle (M: 27510 μm^2 SD: 2600 μm^2) — Conventional Nozzle (M: 14790 μm^2 SD: 1750 μm^2)
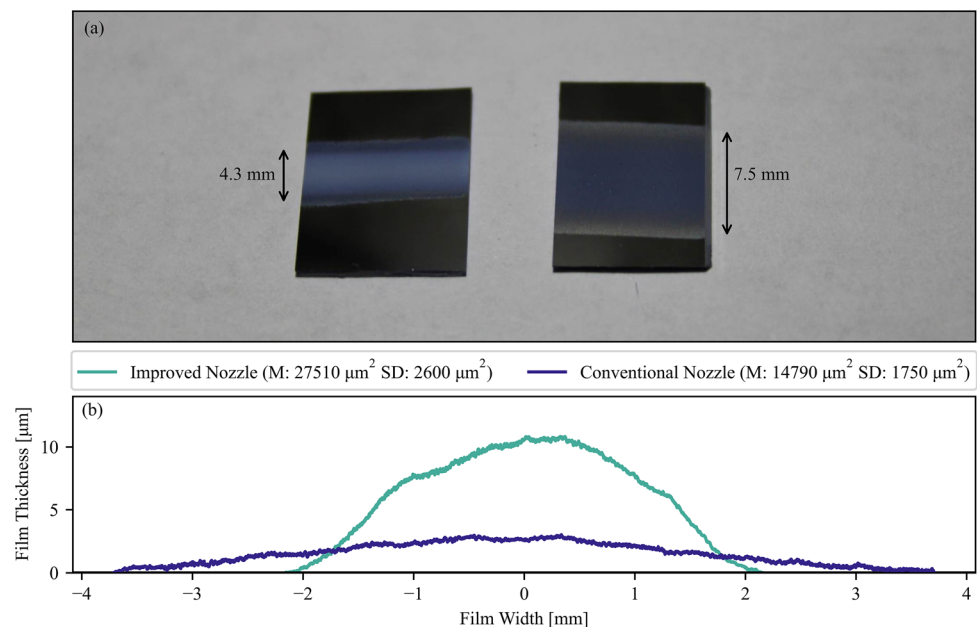
to increase focusing in a nozzle for silver microparticles (Ref 28) and therefore could affect the degree focusing that we observed with MCS. The thermophoretic force could also affect results since it has been shown to slightly decrease particle impact velocities (Ref 29). However, further work is needed before the Saffman lift force and the thermophoretic force can be incorporated into models of MCS because there are limitations with the current formulations of both models. The current implementation of the Saffman lift force is not valid for compressible or rarified flows that are present for MCS conditions (Ref 30, 31), and the data upon which the thermophoretic model is based are from experimental data from low-velocity laminar flows that have not been validated for conditions similar to those found in MCS (Ref 32). Thus, including the effects of these forces is beyond the scope of the present study.

The predicted particle velocities in this and previous related work assume that the particles used in MCS are solid, spherical particles. However, in practice, the micron-to sub-micron-sized ceramic particles used in MCS are susceptible to agglomeration due to Van der Walls or electrostatic forces between the particles, and the severity of agglomeration increases for the ultrafine particles that are enabled by use of a pressure relief channel nozzle design. Filtering and size classification (Ref 8) have been used previously to solve this problem by removing agglomerates from the deposited powder so that only individual particles are deposited. Although effective, filtering reduces the overall efficiency of the deposition process since a large fraction of the powder is removed before it is fed into this system and thus alternatives to filtering that can achieve higher utilization of the powder are desirable.

In this paper, we utilized strong shear forces introduced in deagglomerator located upstream of the nozzle to produce a mixture of individual particles and small agglomerates, as shown Fig. 7. Compared to individual, solid particles, small agglomerates are also more strongly slowed by the bow shock due to their increased drag-to-mass ratio. Thus, the calculated benefits of using the improved nozzle design to reduce particle slowing could be even greater for agglomerates than predicted for individual particles. It follows that the use of the improved nozzle design may allow small agglomerates, which have low relative densities compared to solid particles and would be strongly affected by the dense, stagnant gas downstream of the bow shock, to deposit and contribute to film formation.

Another method that has been utilized previously for increasing the deposition efficiency is to eliminate the finer particles in the size distribution through a combination of heat treatment and ball milling of the powder prior to deposition (Ref 6, 33, 34). The heat treatment increases the density of the agglomerates and reduces the drag-to-mass ratio, making them less susceptible to particle slowing in the bow shock. However, even with relatively monosized powders, the impact velocity produced with a conventional nozzle must be carefully selected; if the velocity is too low, the particles elastically rebound rather than depositing and if the velocity is too high, the larger momentum upon impact for larger particles that are moving at high velocity erodes the substrate and film. This damage to the substrate and film results in reduced deposition rates and poorer film quality (Ref 35).

We previously showed that the use of a pressure relief channel nozzle with N_2 gas was effective at depositing sub-micron scale YSZ powders that had a distribution in particle and agglomerate sizes without the need for powder heat treatments (Ref 14). However, the produced films were porous, indicating that the impact velocities were high enough to deposit the smallest particles, but still too low to deform the particles sufficiently to produce dense films. In this study, higher impact velocities were attained for fine particles. The impact velocity was increased from approximately 500 m/s to over 1200 m/s for a 50 nm YSZ particle by using He gas in combination with the pressure relief channel nozzle design. The analysis predicted that using this combination, particles in the size range from 20 to 100 nm can be deposited at velocities of greater than 1000 m/s. SEM images of film cross sections revealed films produced from particles and small agglomerates with a primary particle size of 40 nm exhibited minimal porosity. These results suggest that the use of finer particle sizes in combination with a pressure relief channel nozzle design and He gas allows the deposition of dense films without significant film erosion and without the need for size filtering or powder heat treatments.

The results of the analysis revealed that there is a trade-off that arises with the pressure relief channel nozzle design. For example, Figs. 6 and 7 show that the use of ultrafine powders enabled by the pressure relief channel nozzle results in particle defocusing by the finest particle sizes and overfocusing for particles 100 nm and larger, leading to decreased impact velocities and removal of particles through the channels. While this is the first example that we are aware of for a nozzle geometry designed to increase impact velocities for ultrafine powders, particle focusing was not considered in this nozzle design. There have been many previous studies of nozzle geometries aimed at improving particle focusing or optimizing bow shock behavior. For example, aerodynamic focusing by using multiple flat nozzles placed in series has shown to be effective at focusing particles down to as fine as 5 nm (Ref 36, 37). It is notable that the same trade-off between focusing and particle impact velocity occurs for these nozzle geometries. This is because multiple nozzles

placed in series focus the aerosol, but successively lower upstream pressures reduce the degree to which the particles can be accelerated. For MCS, nozzles have been designed largely to eliminate adverse shock wave behavior that can result in wide variation in particle behavior (Ref 38, 39). These nozzles, while optimized for the particle size ranges typically used in MCS, have the same limitations on particle size as the conventional converging–diverging nozzle presented in this work.

While this work demonstrates significant increases in deposition efficiency for an ultrafine powder when using a pressure relief channel nozzle, much has yet to be understood about the effects of various process parameters. The differences in deposition efficiencies between the two films as shown in Figs. 9 and 10 may be the result of at least one the films that have reached a limiting thickness. The uniform thickness and minimal visible porosity in the film deposited with the pressure relief channel nozzle suggest that it may be possible to further increase the film thickness with additional deposition. The apparently higher porosity and uneven thickness of the film deposited with the conventional converging–diverging nozzle suggest that this film thickness may already be limited by the lack of deposition of fine particles. Future work to examine the effects of various process parameters is necessary to fully understand the benefits and limitations of the pressure relief channel nozzles.

Conclusions

The use of a pressure relief channel nozzle in combination with a helium carrier gas is shown to increase the deposition efficiency and improve film quality when compared to films deposited using a conventional converging–diverging nozzle. This combination allows 8YSZ particles as small as 10 nm to be deposited at impact velocities > 800 m/s by increasing gas velocities to ∼ 1500 m/s and minimizing gas density in the stagnation region. While some fraction of particles exits the nozzle through the pressure relief channel and does not impact on the substrate, apparent density and uniformity of the deposited films are improved when compared to a conventional converging–diverging nozzle, and an increase in deposition efficiency of > 180% is observed.

References

1. J. Akedo and M. Lebedev, Microstructure and Electrical Properties of Lead Zirconate Titanate (Pb(Zr52/Ti48)O3) Thick Films Deposited by Aerosol Deposition Method, *Jpn. J. Appl. Phys.*, 1999, **38**(9S), p 5397. https://doi.org/10.1143/JJAP.38.5397
2. J. Akedo and M. Lebedev, Influence of Carrier Gas Conditions on Electrical and Optical Properties of Pb(Zr, Ti)O3 Thin Films Prepared by Aerosol Deposition Method, *Jpn. J. Appl. Phys.*, 2001, **40**(9S), p 5528. https://doi.org/10.1143/JJAP.40.5528
3. J. Akedo, Aerosol Deposition Method for Fabrication of Nano Crystal Ceramic Layer, *Mater. Sci. Forum*, 2004, **449–452**, p 43–48. https://doi.org/10.4028/www.scientific.net/MSF.449-452.43
4. J.J.H. McCallister, M.D. Gammage, J.W. Keto, M.F. Becker, and D. Kovar, Influence of Agglomerate Morphology on Micro Cold Spray of Ag Nanopowders, *J. Aerosol Sci.*, 2021, **151**, p 105648. https://doi.org/10.1016/j.jaerosci.2020.105648
5. J.J.H. McCallister, J.W. Keto, M.F. Becker, and D. Kovar, Influence of Normal Velocity on Microstructure and Density of Films Produced by Nanoparticle Impact, *AIP Adv.*, 2019, **9**(3), p 35226. https://doi.org/10.1063/1.5080949
6. D. Hanft, M. Bektas, and R. Moos, Powder Pre-Treatment for Aerosol Deposition of Tin Dioxide Coatings for Gas Sensors, *Materials*, 2018, **11**(8), p 1342. https://doi.org/10.3390/ma11081342
7. H. Kwon, H. Park, and C. Lee, Roles of Particle Size Distribution in Bimodal Feedstocks on the Deposition Behavior and Film Properties in Vacuum Kinetic Spraying, *J. Therm. Spray Technol.*, 2018, **27**(5), p 857–869.
8. J. Akedo, Room Temperature Impact Consolidation (RTIC) of Fine Ceramic Powder by Aerosol Deposition Method and Applications to Microdevices, *J. Therm. Spray Technol.*, 2008, **17**(2), p 181–198.
9. A.H. Moyers, D.W. Davies, M.F. Becker, and D. Kovar, A Molecular Dynamics Survey Study of Impact-Induced Amorphization in Yttria Nanoparticles, *J. Aerosol Sci.*, 2022, **162**, p 105976. https://doi.org/10.1016/j.jaerosci.2022.105976
10. D.W. Davies, A.H. Moyers, M.D. Gammage, J.W. Keto, M.F. Becker, and D. Kovar, Deformation and Film Formation Mechanisms during High Velocity Impact of Silicon Carbide Nanoparticles, *J. Aerosol Sci.*, 2022, **163**, p 105997. https://doi.org/10.1016/j.jaerosci.2022.105997
11. G. Song, H. Yang, and C.J. Hogan, Thermal Energy Evolution and Mechanical Deformation of Monocrystalline Yttria-Stabilized Zirconia Nanoparticles in Aerosol Deposition Processes, *Appl. Surf. Sci.*, 2022, **585**, p 152603.
12. S.G. Bierschenk, M.F. Becker, and D. Kovar, Effect of an Oxide Layer on High Velocity Impact of Tantalum Particles

Characterized Using Molecular Dynamics, *Appl. Surf. Sci.*, 2023, **640**, p 158394. https://doi.org/10.1016/j.apsusc.2023.158394

13. S. Lee, J.H. Park, C.G. Park, D.-Y. Jeong, and N.-M. Hwang, Generation of Positively Charged Nanoparticles by Fracto-Emission and Their Deposition into Films during Aerosol Deposition, *Appl. Surf. Sci.*, 2022, **593**, p 153466.

14. S.G. Bierschenk and D. Kovar, A Nozzle Design for Mitigating Particle Slowing in the Bow Shock Region during Micro-Cold Spray of 8YSZ Films, *J. Aerosol Sci.*, 2024, **179**, p 106360. https://doi.org/10.1016/j.aerosci.2024.106360

15. D. Hanft, J. Exner, M. Schubert, T. Stöcker, P. Fuierer, and R. Moos, An Overview of the Aerosol Deposition Method: Process Fundamentals and New Trends in Materials Applications, *J. Ceram. Sci. Technol.*, 2015, **6**(3), p 147–182. https://doi.org/10.4416/JCST2015-00018

16. C. AB, "CFD Module User's Guide COMSOL Multiphysics® v. 5.6.," COMSOL AB, 2022, www.comsol.com.

17. S.G. Bierschenk, M.F. Becker, and D. Kovar, Gas and Ceramic Particle Velocities for Micro-Cold Spray, *J. Aerosol Sci.*, 2023, **169**, p 106113. https://doi.org/10.1016/j.aerosci.2022.10611

18. COMSOL AB, "CFD Module User's Guide COMSOL Multiphysics® v. 5.6.," COMSOL AB, 2022, www.comsol.com.

19. P. Spalart and S. Allmaras, A one-equation turbulence model for aerodynamic flows, in *30th Aerospace Sciences Meeting and Exhibit*, American Institute of Aeronautics and Astronautics, 1992. https://doi.org/10.2514/6.1992-439

20. R. Paciorri, W. Dieudonne, G. Degrez, J.-M. Charbonnier, H. Deconinck, R. Paciorri, W. Dieudonne, G. Degrez, J.-M. Charbonnier, and H. Deconinck, Validation of the spalart-allmaras turbulence model for application in hypersonic flows, in *28th Fluid Dynamics Conference*, American Institute of Aeronautics and Astronautics, 2012. https://doi.org/10.2514/6.1997-2023

21. H. Park, H. Kwon, and C. Lee, Inflight Particle Behavior in the Vacuum Kinetic Spray Process, *J. Therm. Spray Technol.*, 2017, **26**(7), p 1616–1631. https://doi.org/10.1007/s11666-017-0614-x

22. S.D. Johnson, D. Schwer, D.-S. Park, Y.-S. Park, and E.P. Gorzkowski, Deposition Efficiency of Barium Hexaferrite by Aerosol Deposition, *Surf. Coat. Technol.*, 2017, **332**, p 542–549. https://doi.org/10.1016/j.surfcoat.2017.06.085

23. H. Katanoda and K. Matsuo, Gasdynamic Simulation of Aerosol Deposition Method, *Mater. Trans.*, 2006, **47**(7), p 1620–1625.

24. H. Katanoda, M. Fukuhara, and N. Iino, Numerical Simulation on Impact Velocity of Ceramic Particles Propelled by Supersonic Nitrogen Gas Flow in Vacuum Chamber, *Mater. Trans.*, 2007, **48**(6), p 1463–1468.

25. H. Park, H. Kwon, Y. Kim, and C. Lee, Computational Research on Factors Affecting Particle Velocity in a Vacuum Kinetic Spray Process, *J. Therm. Spray Technol.*, 2019, **28**(8), p 1945–1958. https://doi.org/10.1007/s11666-019-00941-6

26. C. Li, N. Singh, A. Andrews, B.A. Olson, T.E. Schwartzentruber, and C.J. Hogan, Mass, Momentum, and Energy Transfer in Supersonic Aerosol Deposition Processes, *Int. J. Heat Mass Transf.*, 2019, **129**, p 1161–1171.

27. D. Davies, *Systematic Study and Characterization of Silicon Carbide Films Produced via Micro Cold Spray (Austin)*, (The University of Texas at Austin, 2023).

28. S. Bhattacharya, A. Lutfurakhmanov, J.M. Hoey, O.F. Swenson, Z. Mahmud, and I.S. Akhatov, Aerosol Flow Through a Converging-Diverging Micro-Nozzle, *Nonlinear Engineering*, 2013, **2**(3–4), p 103–112. https://doi.org/10.1515/nleng-2013-0020

29. A. Zabihi Yeganeh, M. Jadidi, C. Moreau, and A. Dolatabadi, Numerical Modeling of Aerosol Deposition Process, *Surf. Coat. Technol.*, 2019, **370**, p 269–287. https://doi.org/10.1016/j.surfcoat.2019.04.094

30. P.G. Saffman, The Lift on a Small Sphere in a Slow Shear Flow, *J. Fluid Mech.*, 1965, **22**(2), p 385–400.

31. A. Kudryavtsev, A. Shershnev, and O. Rybdylova, Numerical Simulation of Aerodynamic Focusing of Particles in Supersonic Micronozzles, *Int. J. Multiph. Flow*, 2019, **114**, p 207–218.

32. L. Talbot, R.K. Cheng, R.W. Schefer, and D.R. Willis, Thermophoresis of Particles in a Heated Boundary Layer, *J. Fluid Mech.*, 1980, **101**(4), p 737–758.

33. J. Exner, M. Schubert, D. Hanft, J. Kita, and R. Moos, How to Treat Powders for the Room Temperature Aerosol Deposition Method to Avoid Porous, *Low Strength Ceramic Films, J Eur Ceram Soc*, 2019, **39**(2–3), p 592–600.

34. K. Mihara, T. Hoshina, H. Kakemoto, H. Takeda, and T. Tsurumi, Effects of Pretreatments on Deposition Rate of Films in Aerosol Deposition Method, *Key Eng. Mater.*, 2009, **421–422**, p 165–168.

35. D.-W. Lee, H.-J. Kim, Y.-H. Kim, Y.-H. Yun, and S.-M. Nam, Growth Process of α-Al2O3 Ceramic Films on Metal Substrates Fabricated at Room Temperature by Aerosol Deposition, *J. Am. Ceram. Soc.*, 2011, **94**(9), p 3131–3138. https://doi.org/10.1111/j.1551-2916.2011.04493.x

36. H.L. Lu, L. Li, X.H. Liang, J.J. Wang, N.Y. Liu, and Z.T. Chen, Study of Aerodynamic Focusing Lens Stacks (ALS) for Long Focal Length Aerosol-Assisted Focused Chemical Vapor Deposition (AAFCVD), *RSC Adv.*, 2021, **11**(8), p 4425–4437.

37. X. Wang, F.E. Kruis, and P.H. McMurry, Aerodynamic Focusing of Nanoparticles: I Guidelines for Designing Aerodynamic Lenses for Nanoparticles, *Aerosol Sci. Technol.*, 2005, **39**(7), p 611–623.

38. J.-J. Park, M.-W. Lee, S.S. Yoon, H.-Y. Kim, S.C. James, S.D. Heister, S. Chandra, W.-H. Yoon, D.-S. Park, and J. Ryu, Supersonic Nozzle Flow Simulations for Particle Coating Applications: Effects of Shockwaves, Nozzle Geometry, Ambient Pressure, and Substrate Location upon Flow Characteristics, *J. Therm. Spray Technol.*, 2011, **20**(3), p 514–522.

39. M.W. Lee, J.J. Park, D.Y. Kim, S.S. Yoon, H.Y. Kim, D.H. Kim, S.C. James, S. Chandra, T. Coyle, J.H. Ryu, W.H. Yoon, and D.S. Park, Optimization of Supersonic Nozzle Flow for Titanium Dioxide Thin-Film Coating by Aerosol Deposition, *J. Aerosol Sci.*, 2011, **42**(11), p 771–780. https://doi.org/10.1016/j.jaerosci.2011.07.006